

## Article

# Microstructure and Mechanical Properties of Laser Additive Manufactured H13 Tool Steel

Karel Trojan <sup>1,\*</sup>, Václav Ocelík <sup>2</sup>, Jiří Čapek <sup>1</sup>, Jaroslav Čech <sup>3</sup>, David Canelo-Yubero <sup>4,5</sup>, Nikolaj Ganev <sup>1</sup>, Kamil Kolařík <sup>1</sup> and Jeff T. M. De Hosson <sup>2</sup>

<sup>1</sup> Department of Solid State Engineering, Faculty of Nuclear Sciences and Physical Engineering, Czech Technical University in Prague, Trojanova 13, 120 00 Prague, Czech Republic; jiri.capek@fjfi.cvut.cz (J.Č.); nikolaj.ganev@fjfi.cvut.cz (N.G.); kamil.kolarik@fjfi.cvut.cz (K.K.)

<sup>2</sup> Department of Applied Physics, Zernike Institute for Advanced Materials, Faculty of Science and Engineering, University of Groningen, Nijenborgh 4, 9747 AG Groningen, The Netherlands; v.ocelik@rug.nl (V.O.); j.t.m.de.hosson@rug.nl (J.T.M.D.H.)

<sup>3</sup> Department of Materials, Faculty of Nuclear Sciences and Physical Engineering, Czech Technical University in Prague, Trojanova 13, 120 00 Prague, Czech Republic; jaroslav.cech@fjfi.cvut.cz

<sup>4</sup> Neutron Physics Department, Nuclear Physics Institute ASCR, 250 68 Prague, Czech Republic; caneloyubero@ujf.cas.cz

<sup>5</sup> Helmholtz-Zentrum Hereon, Institute of Materials Physics, Max-Planck-Straße 1, 21502 Geesthacht, Germany

\* Correspondence: karel.trojan@fjfi.cvut.cz; Tel.: +420-224-358-624

**Abstract:** Hot working tool steel (AISI H13) is one of the most common die materials used in casting industries. A die suffers from damage due to friction and wear during its lifetime. Therefore, various methods have been developed for its repair to save costs to manufacture a new one. A great benefit of laser additive manufacturing (cladding) is the 3D high production rate with minimal influence of thermal stresses in comparison with conventional arc methods. Residual stresses are important factors that influence the performance of the product, especially fatigue life. Therefore, the aim of this contribution is to correlate the wide range of results for multilayer cladding of H13 tool steel. X-ray and neutron diffraction experiments were performed to fully describe the residual stresses generated during cladding. Additionally, in-situ tensile testing experiments inside a scanning electron microscope were performed to observe microstructural changes during deformation. The results were compared with local hardness and wear measurements. Because laser cladding does not achieve adequate accuracy, the effect of necessary post-grinding was investigated. According to the findings, the overlapping of beads and their mutual tempering significantly affect the mechanical properties. Further, the outer surface layer, which showed tensile surface residual stresses and cracks, was removed by grinding and surface compressive residual stresses were described on the ground surface.

**Keywords:** laser additive manufacturing; laser cladding; AISI H13 tool steel; microstructure; residual stresses; electron diffraction; X-ray diffraction; neutron diffraction; in-situ tensile testing



**Citation:** Trojan, K.; Ocelík, V.; Čapek, J.; Čech, J.; Canelo-Yubero, D.; Ganev, N.; Kolařík, K.; De Hosson, J.T.M. Microstructure and Mechanical Properties of Laser Additive Manufactured H13 Tool Steel. *Metals* **2022**, *12*, 243. <https://doi.org/10.3390/met12020243>

Academic Editors: Wei Zhou and Guijun Bi

Received: 3 January 2022

Accepted: 24 January 2022

Published: 27 January 2022

**Publisher's Note:** MDPI stays neutral with regard to jurisdictional claims in published maps and institutional affiliations.



**Copyright:** © 2022 by the authors. Licensee MDPI, Basel, Switzerland. This article is an open access article distributed under the terms and conditions of the Creative Commons Attribution (CC BY) license (<https://creativecommons.org/licenses/by/4.0/>).

## 1. Introduction

Additive manufacturing technologies are currently widely explored due to their capability of reducing the amount of material needed and increasing the precision in complex geometries of components. Laser cladding is one of the methods, where the power density of a laser beam is applied to melt and deposit the material. Powders are mainly used for the additive production of metals, which are subsequently melted through laser radiation and form a newly added volume through a layered structure. There are two approaches; the first one uses the so-called powder bed, where the material is applied to the surface and the laser beam subsequently remelts only the given shape for each layer. This method, known as selective laser melting (SLM), achieves higher accuracy, but the process is very slow [1]. The second approach uses a powder feeder, which is directed into

the laser beam; the molten metal then solidifies and forms a new clad layer. This method, referred to as laser cladding or sometimes laser metal deposition (LMD), is less accurate, but the cladding speed is several times faster than the SLM [2].

AISI H13 hot working tool steel is one of the most common materials of a die and mould used in casting industries. A die suffers from damage due to friction and wear during its lifetime. Therefore, various methods have been developed for its repair to save costs of manufacturing a new one [3]. Another effort is to use dies with conformal cooling where the cooling channels can be closer to the surface and thus better control the cooling rate. Complex cooling channels cannot be created by conventional methods, such as drilling [4]. A great benefit of laser cladding in this field is the 3D high production rate of a new volume with almost any shape and with minimal heat influence due to low heat input into the surrounding material. The lower heat input reduces the deformation of the die or the deterioration of the material properties due to tempering. Laser cladding, therefore, enables production and repairs without additional pre- and post-cladding thermal treatments [5]. A pilot study of the use of H13 tool steel laser cladding for gear repair was described in [6]. However, when cladding multiple layers, the previous layers are thermally affected, which can significantly change their microstructure and mechanical properties [7]. For this reason, not only the cooling rate but also the temperature reached during the cladding of additional layers affects the resulting microstructure [8]. Therefore, it is important to observe and understand the microstructural changes through the thickness of the newly formed material. This knowledge can be used to design a cladding strategy for laser beam deposition of larger volumes.

Orientation imaging microscopy (OIM) maps (phase, crystal orientation, local misorientation, etc.) provide detailed information about the sample microstructure [9]. The microstructure of one clad H13 tool steel layer was reported in [3] by OIM using electron backscatter diffraction (EBSD), where martensite and retained austenite were observed in the clad metal itself. Between martensitic laths, carbides, probably  $M_7C_3$ , where M are different alloying elements, were detected in SEM images. No retained austenite and carbides were observed by X-ray diffraction. Conversely, based on EBSD measurement, it was found that the clad contained retained austenite,  $Mo_2C$  carbide, up to 23 vol. % of  $Cr_{23}C_6$  and  $Cr_7C_3$  carbides and 26 vol. % of VC carbide, which, when converted to weight percentages, corresponded to 20.5 wt. % of  $Cr_{23}C_6$  and  $Cr_7C_3$  carbides, and 19 wt. % VC. Although only a small area of the clad was analysed using the EBSD method, this result did not agree with the overall weight percentage of each alloying element in the used steel, see Table 1 (there is only 5 wt. % of Cr in the steel according to the standard). Furthermore, in [10] more than 36 vol. % of carbides was described in one clad bead using EBSD, which again did not correspond to the chemical composition. Samples prepared by the SLM method based on X-ray diffraction did not contain carbides either in [11]. Therefore, our goal is to verify EBSD microstructural observations and to perform a reliable phase analysis.

**Table 1.** Chemical composition of the AISI H13 steel according to ASTM A681.

Element	Fe	Cr	Mo	Si	V	Mn	C
Weight fraction (wt. %)	balanced	4.75–5.50	1.10–1.75	0.80–1.25	0.80–1.20	0.20–0.60	0.32–0.45

Despite the aforementioned advantages of laser cladding, due to a heterogeneous response of heat conduction and heat dissipation, high residual stresses can be generated in the cladding itself and at the interface between clad and substrate areas as a result of the fast-cooling rates and the difference in thermal expansion coefficients. These residual stresses are formed by a superposition of thermal and transformation processes and can reach high values close to the yield stress of the material. The presence of tensile residual stresses is detrimental in physical processes as, for instance, fatigue or, in combination with defects, promotes brittle fractures [12]. In general, tensile residual stresses arise due to shrinkage, conversely, compressive stresses due to phase transformation, the effect of

which would be dominant depending on the particular situation, i.e., material, geometry and temperature field [13].

The state of residual stresses of a large, clad volume was studied using neutron diffraction in [14]. It was shown that there were compressive residual stress gradients from the surface to a depth of approximately 4 mm. On the contrary, tensile residual stresses were observed at a greater depth, where the hardness also decreased by 200 HV. The compressive stress states in the top layer were assumed to contribute to enhanced fatigue resistance. However, the work did not specify in which direction the main component of residual stress acts [14]. A similar residual stress gradient was described by a numerical simulation using the finite element method, in which a two-layer clad was simulated. In the clad itself in the direction transverse to the beads, the compressive residual stresses were also experimentally confirmed, whereas tensile residual stresses were observed in the substrate [15]. However, in contrast to the latter works, tensile residual stresses were reported in the surface layer when cladding the compositionally similar material CPM 10 V [16]. So far, it is clear that the state of residual stresses has not been thoroughly clarified.

Since laser cladding does not achieve sufficient accuracy, it is always necessary to machine the surface to the final required shape of the component after cladding [5]. It is crucial to determine whether, by post-machining, an area with detrimental mechanical properties reaches the surface. This would lead to a shorter service life. Such a study has not been described in the literature.

Consequently, the objective of this study is to correlate the wide range of results for multilayer cladding, which was prepared by already optimised cladding parameters, see [17,18]. Therefore, the effects of laser cladding on the microstructure and mechanical properties of H13 tool steel using OIM based on EBSD were described. Furthermore, to fully describe the residual stresses generated during cladding, due to the overlapping of individual beads and layers and their mutual tempering, X-ray and neutron diffraction experiments were performed. Additionally, in-situ tensile testing experiments inside a scanning electron microscope were performed to observe microstructural changes during deformation. All obtained results were confronted with local hardness and wear measurements. Finally, yet importantly, the effect of necessary post-grinding was investigated.

Novel results and correlations of this study will find application not only in further research, but also in practice in the production and repair of moulds, dies and other tools made of tool steels.

## 2. Materials and Methods

Laser cladding was carried out using an IPG 3kW YAG (yttrium aluminum garnet) fibre laser (IPG Photonics, Burbach, Germany) with an off-axis powder feeder in the “against hill” condition [2]. A laser power density of  $90 \text{ J/mm}^2$  was applied to form clads in multilayers, see Figure 1. A five-layer sample was formed from six and seven overlapping beads on the substrate made of AISI H11 tool steel. The longitudinal axes of the beads in one layer were 2 mm apart, and the tracks in the next layer were placed in the intermediate positions of the tracks in the previous layer. The powder of AISI H13 tool steel, see Table 1, was used with an average particle diameter of  $94 \pm 24 \mu\text{m}$ . This type of cladding was selected for most analyses. A clad with 14 layers was used for tensile testing.

### 2.1. Metallography

For metallographic analysis, the sample was cut on the T-N plane, then ground, and afterwards, polished. The steel surface was treated by the etchant of 2% Nital (2% nitric acid in ethanol) and Picral (1 g picric acid, 5 mL HCl, 100 mL ethanol). The analysis was performed with the Neophot 32 metallographic microscope (Carl Zeiss Microscopy GmbH, Jena, Germany) and the JEOL JSM-7600F scanning electron microscope (JEOL, Ltd., Akishima, Japan) equipped with a low-angle backscattered electron detector.

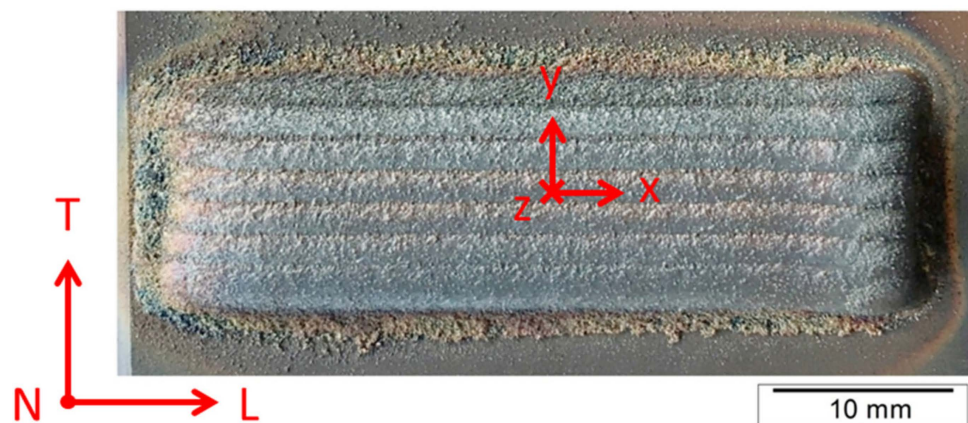


**Figure 1.** Laser clad sample of the AISI H13 tool steel with five layers (top view) with directions marked by N(z), L(x) and T(y) for normal, longitudinal and transverse.

## 2.2. Hardness Tests

Hardness distribution was characterised by the instrumented indentation technique. Tests were carried out on the NHT2 nanoindentation instrument (Anton Paar GmbH, Graz, Austria) with the Berkovich diamond indenter. The indentation cycle consisted of loading to a maximum force of 500 mN, holding at maximum load, and unloading for 30 s, 10 s and 30 s, respectively. Data were evaluated using the Oliver–Pharr method [19,20]. The changes of the hardness of the clad were described from the surface of the clad to the substrate in a cross-section on the T–N plane. Two lines of indents were performed with 75  $\mu\text{m}$  spacing. For hardness measurements of tensile specimens and surface of the ground sample, Vickers hardness tester and maximum load of 10 N were used.

## 2.3. Microstructure

The microstructure of a material is composed of different phases of variable shape, size and distribution (grains, precipitates, dendrites, pores, etc.). In a crystalline material, the microstructure parameters include lattice defects, coherently diffracted domains—crystallites, and preferred grain orientation—texture [21].

The microstructure was described using orientation imaging microscopy (OIM). OIM data were collected using the Philips XL 30 FEG scanning electron microscope (FEI, Eindhoven, The Netherlands) equipped with the TSL OIM system (TexSEM Laboratories, Draper, UT, USA) based on the DigiView 3 camera. The accelerating voltage of 25 kV and 50 nm step size of electron beam scanning were used. A grain boundary was defined as a boundary between two neighbouring scanning points having crystallographic misorientation higher than  $5^\circ$ . All EBSD data were analysed with the TSL OIM Analysis software (version 7.3, TexSEM Laboratories, Draper, UT, USA), and only data points with a confidence index [22] higher than 0.05 were used.

The X'Pert PRO MPD diffractometer (Malvern Panalytical B.V., Almelo, The Netherlands) with cobalt radiation was used for the analyses of microstructure parameters by X-ray diffraction (XRD). The crystallite size and microstrain were determined from the XRD patterns using the Rietveld refinement performed in MStruct software (version 2019, Charles University in Prague, Prague, Czech Republic and Lund University, Lund, Sweden) [23]. Crystallite size and microstrain values were used to calculate dislocation density  $\rho$  using the Williamson and Smallman method [24]. The irradiated volume was defined by the experimental geometry, the effective penetration depth of the X-ray radiation (approx. 5  $\mu\text{m}$ ), and the pinhole size (0.25  $\times$  1 mm).

It has to be noted that the EBSD technique and X-ray diffraction are not able to directly distinguish ferrite and martensite in low carbon steels due to the small tetragonality of martensite.

Further, it is necessary to distinguish between grains and coherently scattering domains, which are referred to as crystallites. A crystallite is considered to be a domain that has an almost monocrystalline structure with a minimum of defects. Therefore, it is clear that a grain where the spatial orientations of individual parts may differ from each other by several degrees is not the same as a crystallite. Thus, the grain consists of an aggregate of randomly slightly rotated crystallites. Microstrain is related to the density of crystal lattice defects and is homogeneous in volume within the size of crystallites [25].

#### 2.4. Residual Stresses Analyses

Surface macroscopic residual stresses were described using X-ray diffraction and the X'Pert PRO MPD diffractometer (Malvern Panalytical B.V., Almelo, The Netherlands) with chromium radiation. The values of surface macroscopic residual stresses were calculated from the lattice deformations, which were determined based on experimental dependencies of  $2\theta$  ( $\sin^2\psi$ ) assuming a bi-axial state of residual stress without gradients in the normal direction, where  $\theta$  is the diffraction angle,  $\psi$  the angle between the sample surface and the diffracting lattice planes [26]. The diffraction angle was determined as the centre of gravity of the  $\text{CrK}\alpha_1\alpha_2$  doublet diffracted by the  $\{211\}$  crystallographic lattice planes of the  $\alpha$ -Fe phase. The X-ray elastic constants  $\frac{1}{2}s_2 = 5.76 \text{ TPa}^{-1}$ ,  $s_1 = -1.25 \text{ TPa}^{-1}$  were used for the stress calculation using software X'Pert Stress (version 2.0, Malvern Panalytical B.V., Almelo, The Netherlands). The sample was analysed by XRD in both the perpendicular T and parallel L directions to the cladding, see Figure 1. The irradiated volume was defined by experimental geometry, the effective penetration depth of the X-ray radiation (approx. 4–5  $\mu\text{m}$ ), and the pinhole size ( $1 \times 1 \text{ mm}$ ).

Neutron diffraction measurements were performed to describe bulk macroscopic residual stresses at Neutron Physics Laboratory of Center of Accelerators and Nuclear Analytical Methods at Nuclear Physics Institute of the Czech Academy of Sciences [27] using the two-axis diffractometer SPN-100 and a 2D  $^3\text{He}$  position-sensitive detector with an active area of  $230 \times 230 \text{ mm}$  and resolution of  $2 \times 2 \text{ mm}$ . The wavelength of the beam was set to  $\lambda = 0.213 \text{ nm}$  with a bent Si(111) crystal monochromator. Cd-slits of  $2 \times 5 \text{ mm}$  were used to shape the incident beam and a radial collimator with a full width at half maximum (FWHM) of 2 mm defined the gauge volume. The sample was placed with its axis vertically for strains in N and T direction, whilst for strains in L directions, the sample was horizontally placed with the L-T plane parallel to the scattering vector. The 2D area detector was positioned at  $2\theta = 63^\circ$  to study the reflection of  $\{110\}$  crystallographic lattice planes of the  $\alpha$ -Fe phase. Five lines were scanned (for three sample orientations) in the normal direction in a T-N plane in the middle of the sample with 2 mm steps for the substrate and 0.5 mm steps in the cladded region. A Gaussian function was used to fit the diffraction peaks with the software StressTex-Calculator (version 2.0.1, Georg-August-Universität Göttingen, Göttingen, Germany) [28].

Bulk residual stresses in L, N and T directions were calculated with Hooke's law [29] using Young's modulus  $E = 214.9 \text{ GPa}$  and Poisson's ratio  $\nu = 0.242$  corresponding to the  $\{110\}$  plane calculated using the program XEC (version 1.0, Hochschule für Technik und Wirtschaft des Saarlandes, Saarbrücken, Germany) by Wern [30]. Measurements were performed at the middle in the longitudinal direction; therefore, a homogeneous distribution of residual stresses in this region was assumed and stresses in the transversal direction were self-equilibrated. This assumption is based on the requirement that force and moment must balance across any selected cross-section. In absence of confidence stress-free references for both substrate and cladded regions, the equilibrium conditions were applied. Therefore, scanned lines in the substrate were used to calculate the stress-free reference for this part. With the scanned line at the centre (where the cladded volume is higher), the stress-free reference of the cladded region was calculated assuming a linear dependence across the heat-affected zone from the substrate to the cladded region.

### 2.5. Tensile Testing

Tensile testing was performed in a scanning electron microscope, which was equipped with the Kammrath & Weiss 5 kN Tensile/Compression Module stage (Kammrath & Weiss GmbH, Schwerte, Germany). Sample elongation was obtained from the jaw movement and the displacement rate of 5  $\mu\text{m/s}$  was used. For tensile testing, a larger volume was cladded above the same substrate made of AISI H11 tool steel. From the cladded volume, specimens with a gauge width and a thickness of 1.6 mm were cut for tensile tests using electric discharge machining. The samples were prepared in a perpendicular (positions 1–4) and parallel (positions 5 and 6) direction to the cladding. For each position, two samples were prepared. Sample A was cut from the upper layers and sample B from the bottom. Sample from the substrate was marked as S.

During in-situ tensile testing, EBSD maps were always collected from the same area (1.3 mm from the final fracture) close to the longitudinal tensile sample axis at different elongations (0, 150, 300 and 500  $\mu\text{m}$ ). From stress–elongation curves, the ultimate tensile strength was deduced. For measurements of the OIM maps, which lasted about 15 min, the jaw movement was stopped, and a slight stress relaxation took place.

### 2.6. Wear Resistance Testing

Wear resistance properties of the laser cladded material were studied using a dry sliding pin on disk test on the CSM HT Tribometer (SMTnet, Portland, OR, USA). The pins were 6 mm in diameter and their side with cladded material was rounded to a ball shape. During the sliding test, the pin was fixed in a pin holder with the pin axis forming a 45° angle to the normal of the disk surface. The pin holder was loaded with 5 N, 10 N and 15 N, respectively, and the rotation speed of the disk was set to a value that corresponds to a sliding speed ranging from 3 to 15 cm/s at ambient temperature. The number of rotations was fixed to reach a sliding distance of 500 m. The disc was made of AISI 5210 (EN 100Cr6) steel with a hardness of  $840 \pm 10 \text{ HV1}$ . Both contact surfaces were polished before the test with 800 grit sandpaper. The worn surface of the pin was analysed with a confocal microscope and the worn volume was evaluated using NFMsurf software (version 6.1, NanoFocus, Oberhausen, Germany). From the volume, the specific wear rate was calculated, which is the ratio of worn volume, load and sliding distance.

## 3. Results and Discussion

The standard tests (metallographic, tensile and hardness) were supplemented by wear tests. These findings were compared with electron, X-ray and neutron diffraction experiments, and provided a detailed description not only of the clad itself but also of the interface of the cladded and base material.

### 3.1. Metallography

In the image of the clad in the T-N plane (Figure 2), several dissimilar areas can be observed. The top layer, which was cladded last, had a significantly different structure from the first layer. Furthermore, a ferritic area occurred between these regions. A transition between the clad and the base material was also observed.

The microstructure was analysed with electron microscopy, see Figure 3. It is assumed that  $\delta$ -ferrite was completely transformed to the austenite during peritectic transformation. In the top layer (Figure 3a), the martensitic structure with a low volume fraction of bainite predominated. An  $\alpha$ -ferrite was found at the boundaries (and rarely also inside) of the prior austenitic grains. Retained austenite could also be observed in the structure; furthermore, cracks could be found on the surface (Figure 4a), probably caused by cooling. In the area with mostly ferritic structure (Figure 3b), ferrite was found and mostly bainite with a low volume fraction of martensite. Fine carbides were present, see Figure 4b. The presence of ferrite in the microstructure will have a significant effect on the decrease in hardness. The first cladded layer (Figure 3c) itself consisted of a mixture of martensite and bainite, acicular ferrite and retained austenite. The upper part of the interface was martensitic with more

pronounced bainitic regions and the lower part of the interface, the heat-affected zone, was strongly tempered, so there was a large number of carbides, ferrite, martensite–austenite and isolated islands of pearlitic colonies. Finally, the base material (Figure 3d) consisted of tempered martensite. Fine carbides were found in the matrix and along the boundaries of the primary austenitic grains.

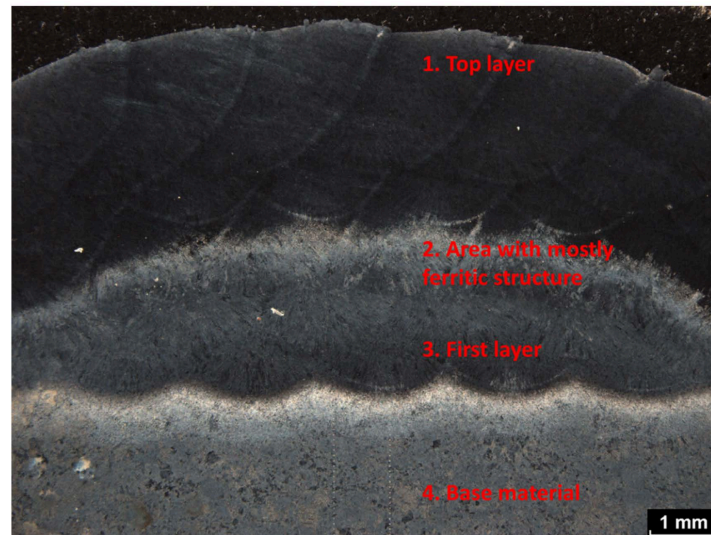


**Figure 2.** Macro image of the clad with marked areas that differ significantly.

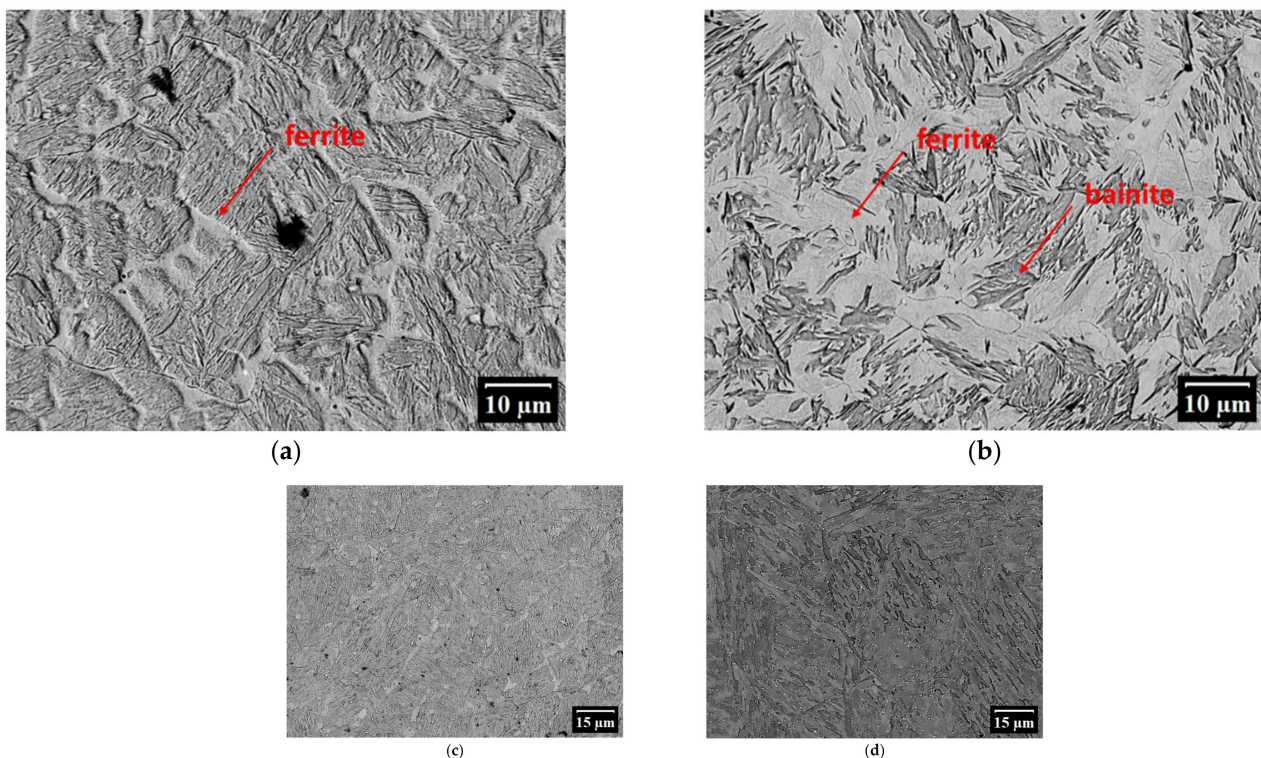


**Figure 3.** Microstructure of: (a) Top layer with a martensitic structure with ferritic envelopes; (b) Area with mostly ferritic structure and bainite with a low volume fraction of martensite; (c) First cladded layer with a mixture of martensite and bainite, acicular ferrite and retained austenite; (d) Base material with tempered martensite and fine carbides.

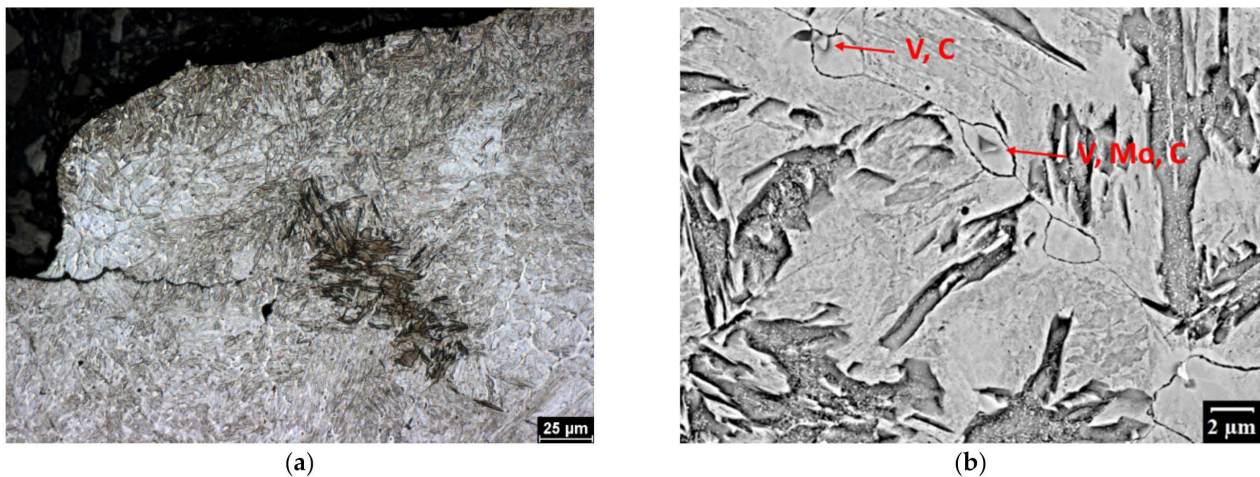


**Figure 4.** Microstructure of: (a) Top layer with a crack; (b) Area with mostly ferritic structure and fine carbides.

### 3.2. Hardness

The hardness of the clad to a depth of approximately 2.5 mm from the surface, which corresponded to the last two layers, was around 700 HV, see Figure 5. This was followed by a significant drop in hardness of 200 HV reaching its minimum at a depth of 3.3 mm. Subsequently, the hardness rose again to the same level as for the surface. From 5.2 mm, the hardness decreased to 230 HV, which corresponded to the annealed state of H11 steel.

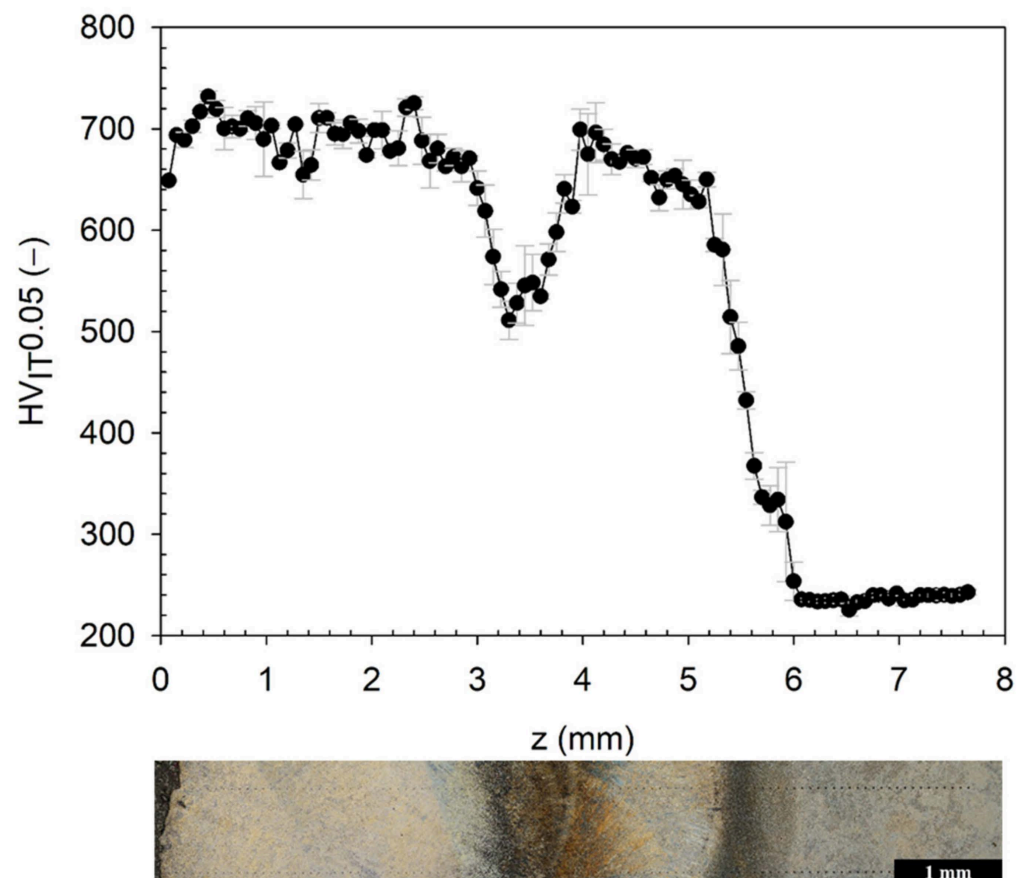


**Figure 5.** Hardness profile from the clad surface to the substrate in comparison with a macro image.

The area with lower hardness corresponded to the darker area on the cross-section, i.e., the area with a mostly ferritic structure which was found in the metallographic study. The change in the microstructure and thus the change in hardness was a consequence of the cladding of the last layers. During cladding of this layer, a very fast quenching occurred within a few seconds, and the hardness should also reach 700 HV. The decrease in hardness resulted from annealing to a temperature of approximately 600 °C [31]. This effect is very interesting, as the second and third layers were annealed due to the heat input from cladding the following layers and not the first one. From this, it can be concluded that the strategy of the cladding process and temperature control can significantly affect the final material properties. On the other hand, it is essential to set the process such that the resulting hardness does not show inhomogeneity close to the surface, because part of the clad volume is always machined. Hardness inhomogeneity on the surface of moulds or dies can significantly reduce the service life.

### 3.3. Microstructure

The microstructure was analysed in the T-N cross-section of the clad using electron and X-ray diffraction.

#### 3.3.1. Electron Diffraction

The microstructure was observed using electron backscatter diffraction (EBSD), see inverse pole figures (IPFs) of the ferritic (bcc) phase in Figure 6. Due to the arrangement inside the electron microscope, the first bead of the penultimate clad layer was analysed. The original austenite grains with a characteristic size of 20–50 µm, which were established during the transition of the melt into a solid phase and which were subsequently transformed into martensitic or bainitic laths, are clearly seen in Figure 6.

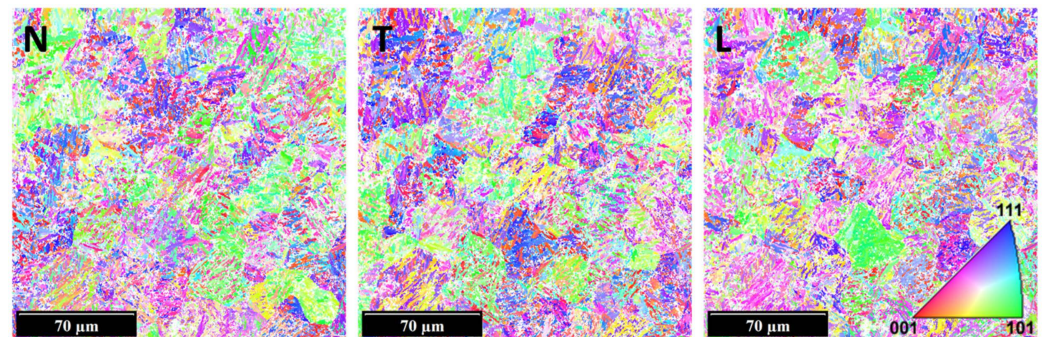


**Figure 6.** Inverse pole figures (IPF maps) of ferritic (bcc) phase for different directions in the selected area, where N, T and L denote the direction.

No other phases were indexed with sufficient confidence in the scanned areas. Retained austenite and carbides of alloying elements can be expected according to previous results, but their confidence index was very small. It is very difficult to numerically distinguish between the cubic lattice of ferrite and  $M_{23}C_6$  carbide (e.g., based on the width of the Kikuchi lines). Information on the local chemical composition can also be used in indexing, but even this route did not lead to better phase resolution. Using automatic indexing resulted in the same errors as mentioned before. At this point, it is worth mentioning that even using X-ray diffraction methods, it was not possible to reliably identify the carbides in the clad. Therefore, the results showed that most alloying elements in the clad (except the area with a mostly ferritic structure) were not in the form of carbides.

#### 3.3.2. X-ray Diffraction

The microstructure parameters were investigated on a cross-section of the clad volume, where a phase analysis of each layer, heat-affected zone (HAZ) and substrate was performed. In the graphs describing the results, see Figure 7, the layers are numbered from

the surface, i.e., the last cladded layer is numbered 1 and the first has a number 5. The HAZ has the number 6 and the substrate 7. Thus, the top layer from the metallographic study corresponds to number 1 and the area with a mostly ferritic structure to numbers 3 and 4.

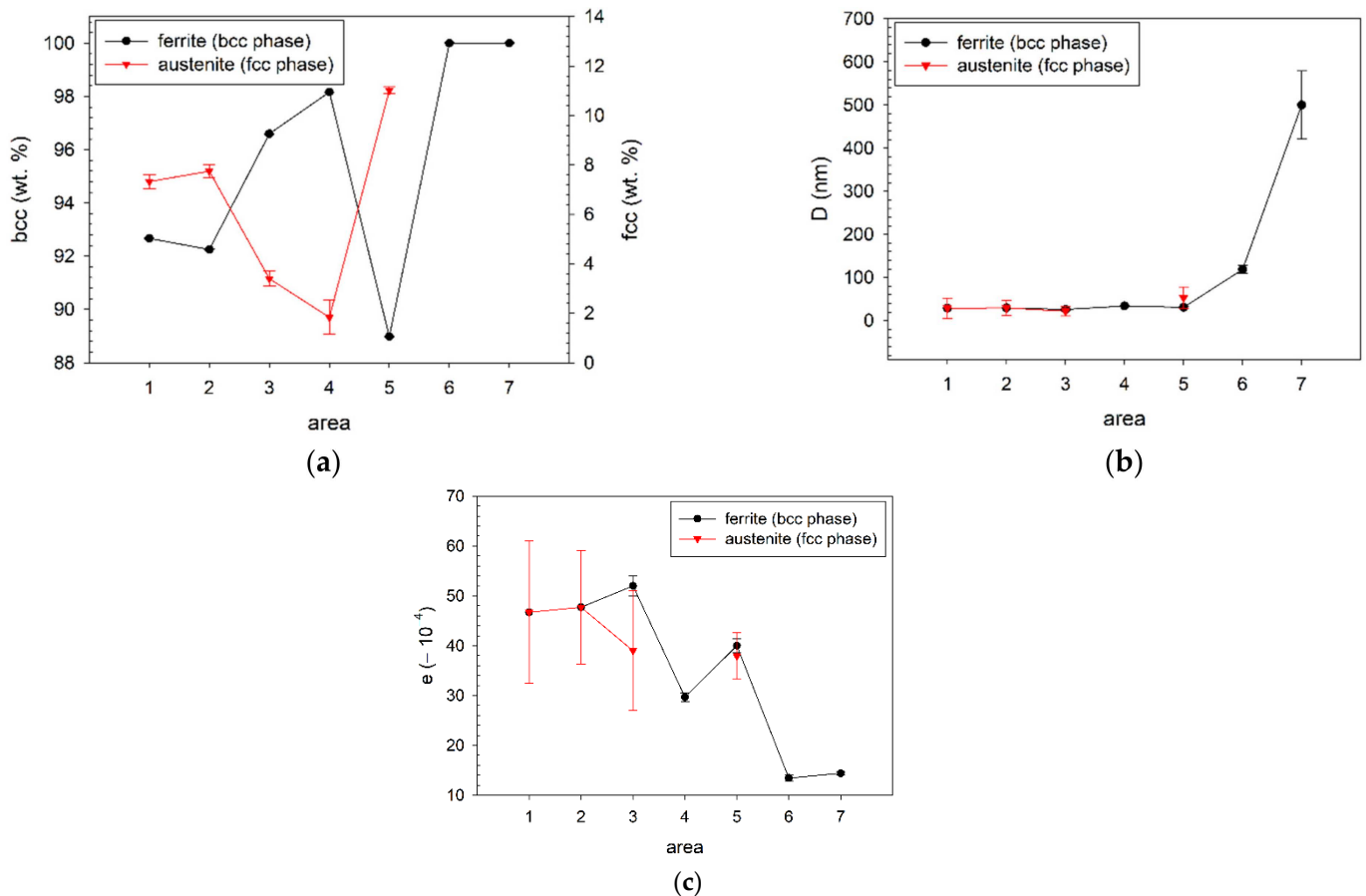


**Figure 7.** Structure of the clad: (a) Phase composition of the cladded layers, where area 1 is the last cladded layer, 5 first one, 6 HAZ and 7 substrate; (b) Crystallite size of the cladded layers; (c) Microstrain of the cladded layers.

According to X-ray phase analysis, the volume fraction of austenite (fcc phase) was the highest in the first cladded layer, approximately 11 wt. %. On the contrary, the lowest volume fraction was in the area with lower hardness, less than 2 wt. %. Using X-ray phase analysis, only ferrite (bcc phase) could be clearly determined in the HAZ and the substrate. Nevertheless, there was an extra maximum on the diffraction pattern of the substrate; it is probably  $M_7C_3$  carbide, where M are different alloying elements. However, based on one maximum, the carbides were not sufficiently characterized by X-ray diffraction as they were very small and probably monocrystalline.

The crystallite size was almost constant for both phases in the cladded layers. In area 4, it was not possible to determine other parameters, because the volume fraction of retained austenite was very low. The crystallite size increased significantly in the HAZ and the substrate, where the value of 500 nm was the set maximum in the MStruct software. Since the H11 tool steel substrate was annealed, it showed a significant coarsening of the grains resulting in larger values of crystallite size.

The microstrain also differed depending on the layer. The microstrain of both phases was identical within the experimental error, again reaching the lowest values in the area with the lowest hardness, which indicates that a higher temperature was reached when cladding the other layers. HAZ and substrate showed lower values as a result of heat treatment.

### 3.4. Residual Stresses

#### 3.4.1. Surface Macroscopic Residual Stresses Obtained Using X-ray Diffraction

Figures 8 and 9 show the surface macroscopic residual stresses in the L direction, i.e., in the cladding direction and the T direction, i.e., transverse. The maps consisted of 33 values and the data were linearly interpolated between them. The average statistical error of the residual stress calculation was approximately 50 MPa for both directions.

#### residual stresses in L direction (MPa)

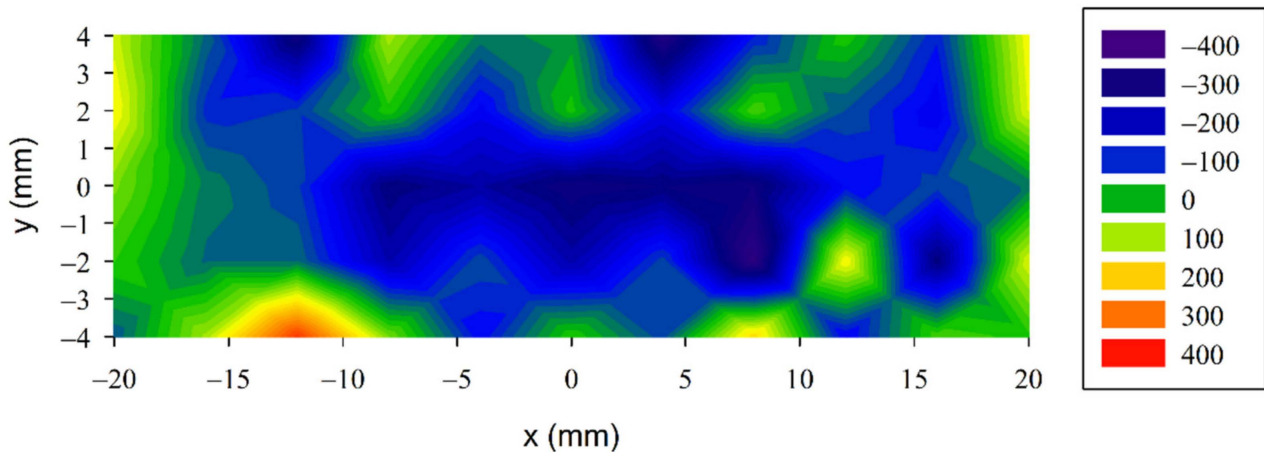


Figure 8. Map of surface macroscopic residual stresses of the clad in the L direction.

#### residual stresses in T direction (MPa)

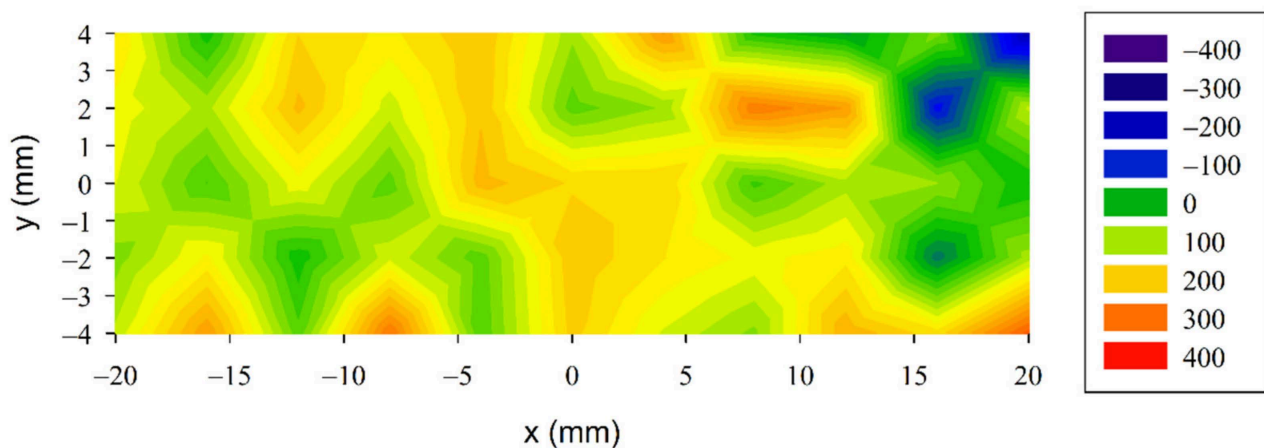


Figure 9. Map of surface macroscopic residual stresses of the clad in the T direction.

Residual stresses reached mainly compressive values in the L direction; only at the edges, there were areas with tensile stresses. On the contrary, tensile residual stresses predominated in the T direction; only a few values had the opposite character. It is appropriate to note that compressive residual stresses had a positive effect on the possible slowing down of crack growth, which spread transversely to the beads. On the contrary, tensile stresses in the T direction reduced fatigue life and promoted crack growth along the beads, which was observed with electron microscopy, see Section 3.1.

This state of residual stress was contrary to expectations since the greatest shrinkage due to cooling occurred in the L direction along the cladding, and in this direction, tensile residual stresses could be expected. At the same time, the compressive residual stresses in the transverse direction were observed in the literature for two-layer cladding [15]. Thus, even with a multilayer clad, the transformation effect prevails over the shrinkage.

### 3.4.2. Bulk Macroscopic Residual Stresses Obtained Using Neutron Diffraction

The state of residual stress was determined using neutron diffraction in the middle of the sample on the T-N ( $yz$ ) plane. Bulk macroscopic residual stresses are plotted in Figure 10, where all three principal components of the stress tensor have been described. Only stresses with the gauge volume totally inside the investigated material are shown; therefore, the values are not up to the edges of the marked clad in the figure. The average statistical error of the residual stress calculation was approximately 13 MPa for all directions.

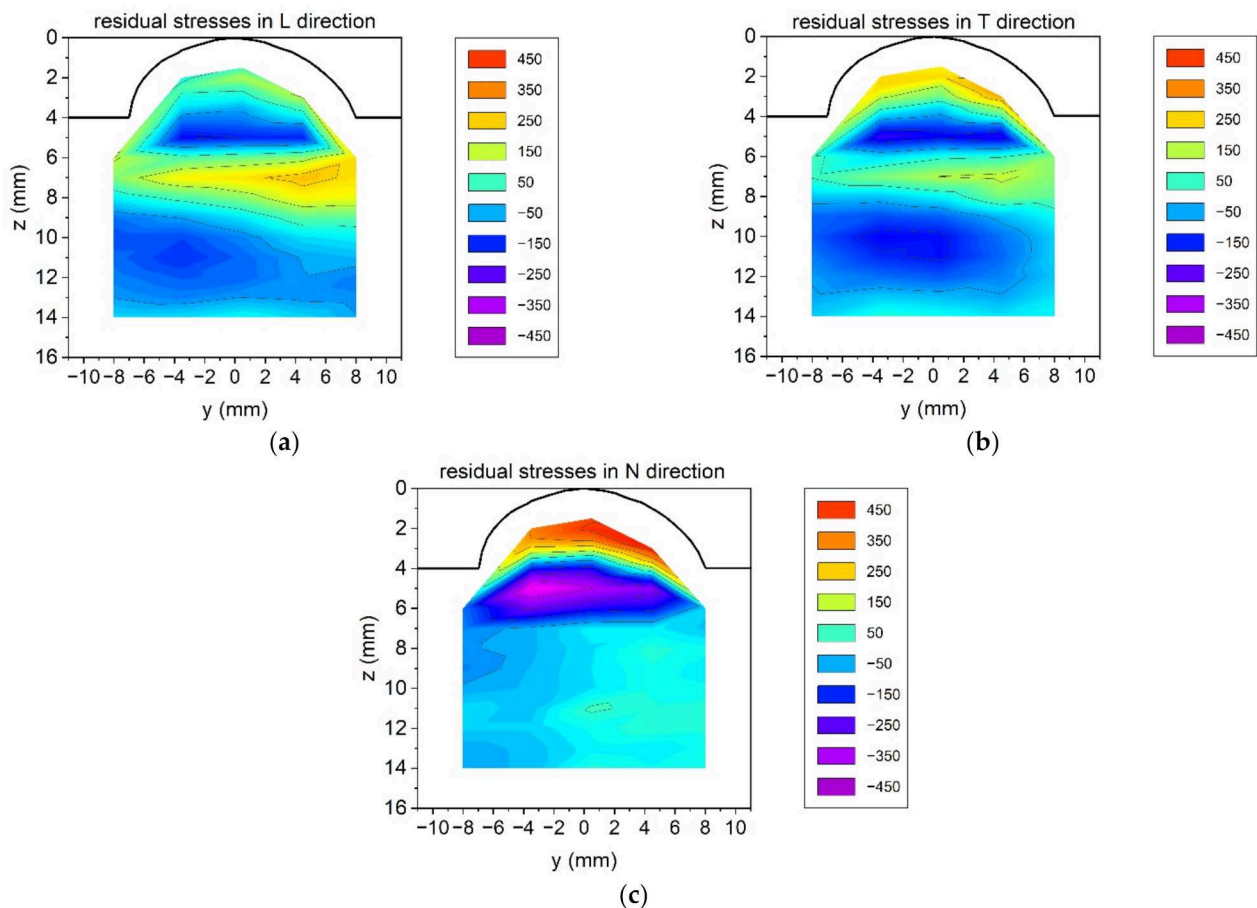


**Figure 10.** Maps of bulk macroscopic residual stresses in the T-N cross-section of the clad in (a) L direction; (b) T direction; (c) N direction.

According to literature studies, cf. [14,15], the maximum residual stresses were located 4 mm below the surface, and the compressive stresses prevailed in the T direction. On the other hand, the substrate exhibited tensile residual stresses. However, according to our results in the clad itself in the T direction, tensile residual stresses predominated; on the contrary, in the substrate compressive residual stresses with one maximum of tensile residual stresses, approximately 3 mm below the surface of the substrate, were determined. Unfavourable tensile stresses close to the surface of the clad were determined in both L and T directions. In the T direction, they reached higher values of up to 250 MPa. This observation agreed with the surface residual stresses, where tensile stresses were described in the T direction. The biggest gradient of residual stresses was found in the N direction—normal to the surface. When the highest tensile values up to 450 MPa reached residual stresses close to the surface.

### 3.5. Tensile Testing

Figure 11 compares values of hardness and tensile strength. Based on these results, a general correlation between the hardness of the sample and tensile strength can be found.

However, the 2A sample had about 200 MPa higher tensile strength than the 1A sample even though they had the same hardness within the errors. On the contrary, the 4A sample exhibited 60 MPa smaller tensile strength than the 2A sample with higher hardness almost by 70 HV1. Differences between B samples cut out perpendicular (1) or parallel (5, 6) to the cladding were not proved. The average tensile strength of the cladded volume was  $1787 \pm 195$  MPa. However, the mean value over more specimens should be used to evaluate appropriate tensile strength but it is questionable when each specimen has a very different hardness.

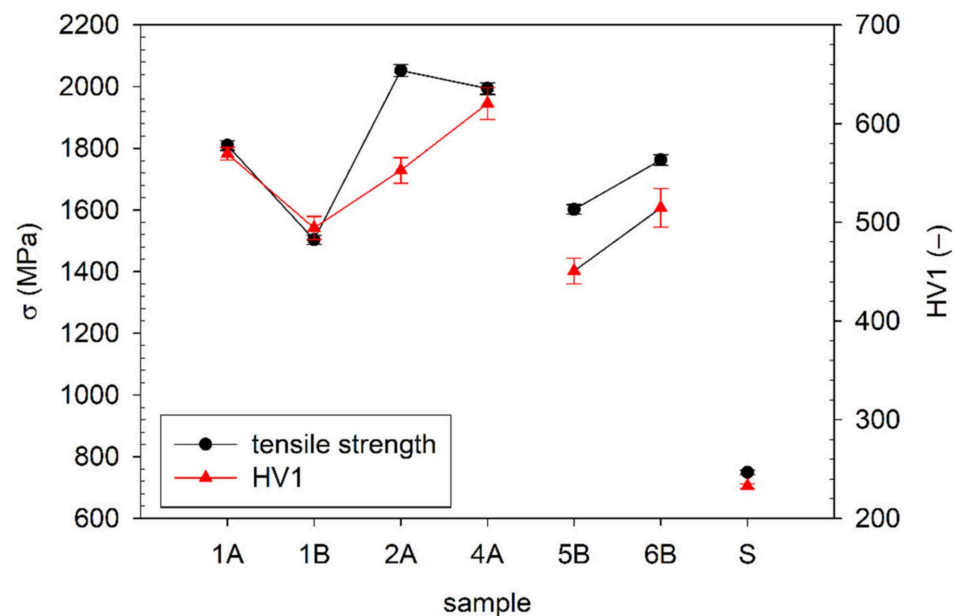


**Figure 11.** Hardness and tensile strength of the selected samples (sample A was cut from the upper layers of the cladded volume and B from the bottom; samples 1–4 were cut in a perpendicular and samples 5–6 parallel direction to the cladding; sample S was cut from the substrate).

Maps of kernel average misorientation (KAM) with the highlighted grain boundaries corresponding to the original austenitic grains are shown in Figure 12. The KAM value is the average misorientation with respect to the first nearest neighbour of a certain point with a  $5^\circ$  maximum. Higher KAM values could be correlated with a higher concentration of geometrically necessary dislocations [22,32], and they are a measure of local strain. Figure 12 shows the highest KAM values for non-loaded sample (average KAM value was  $1.41^\circ$  for  $0 \mu\text{m}$  elongation,  $1.25^\circ$  for  $150 \mu\text{m}$ ,  $1.23^\circ$  for  $300 \mu\text{m}$  and  $1.20^\circ$  for  $500 \mu\text{m}$ ). This interesting result could be explained by the hypothesis that the map for  $0 \mu\text{m}$  elongation showed a local strain due to compressive residual stresses. These stresses were gradually removed in the tensile test; therefore, KAM average value decreased. White areas in Figure 12 are non-indexed points. During the tensile test, the tensile strain was more locally concentrated in areas, which were not indexed in the EBSD experiment, and, therefore, the tensile strain was not properly detected in the EBSD experiment. This hypothesis was confirmed by the measurement of residual stresses by X-ray diffraction, where the tensile residual stresses (approx. 260 MPa) were found in the direction of loading close to the fracture and the compressive (approx.  $-280$  MPa) at a greater distance.

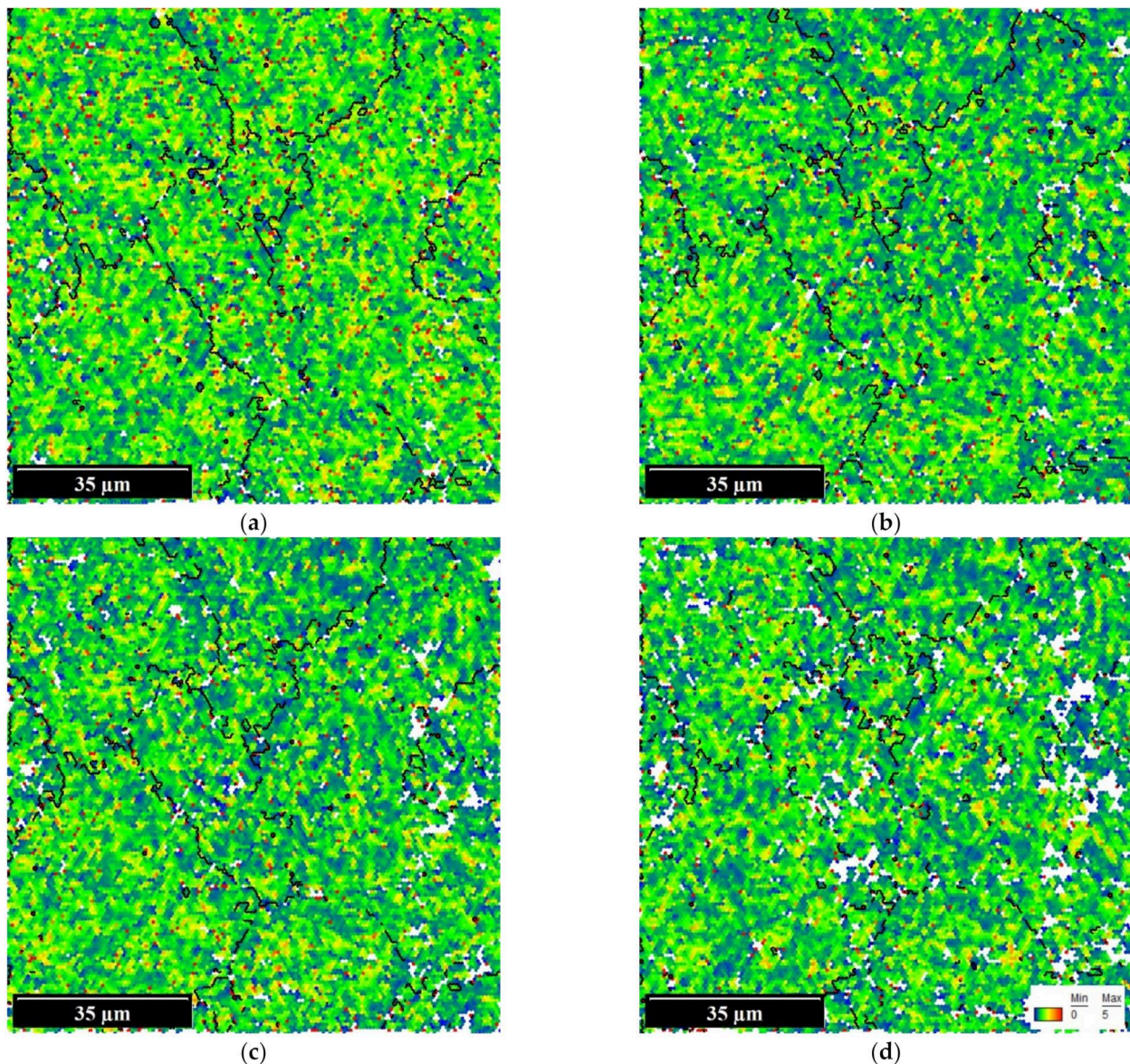


**Figure 12.** KAM maps with highlighted (black lines) grain boundaries of original austenite grains corresponding to an elongation: (a) 0  $\mu\text{m}$ ; (b) 150  $\mu\text{m}$ ; (c) 300  $\mu\text{m}$ ; (d) 500  $\mu\text{m}$ .

### 3.6. Wear Resistance

Figure 13 characterises the dependence of the microhardness of the pins on the specific wear rate. Hardness was obtained from six measurements on the worn surface of the pins. The comparison was made due to the hypothesis that different pin hardness could cause a large variance in wear resistance results within the same sliding speed and load. The correlation between hardness and wear resistance was clear. With increasing hardness, the specific wear rate decreased, which agrees with the conclusions in the available literature [3]. However, it should be realised that increasing hardness also means an increase in the elasticity strain limit and a reduction in ductility, leading to a lowering of fatigue resistance and hence to more brittle failure. For ductile failure, the ratio of hardness to Young's modulus  $E$  is a more suitable parameter for predicting wear resistance. This is understandable since the fracture toughness of the clad coatings defined by the so-called 'critical strain–energy release rate' would be improved by both a low  $E$  and a high hardness [33]. Thus, it can be stated that in this case the resulting wear resistance of the clad volume will be significantly affected by the hardness of the functional surface. In turn,

the hardness is significantly affected by the cladding process and the temperature reached during the cladding of the following layers.

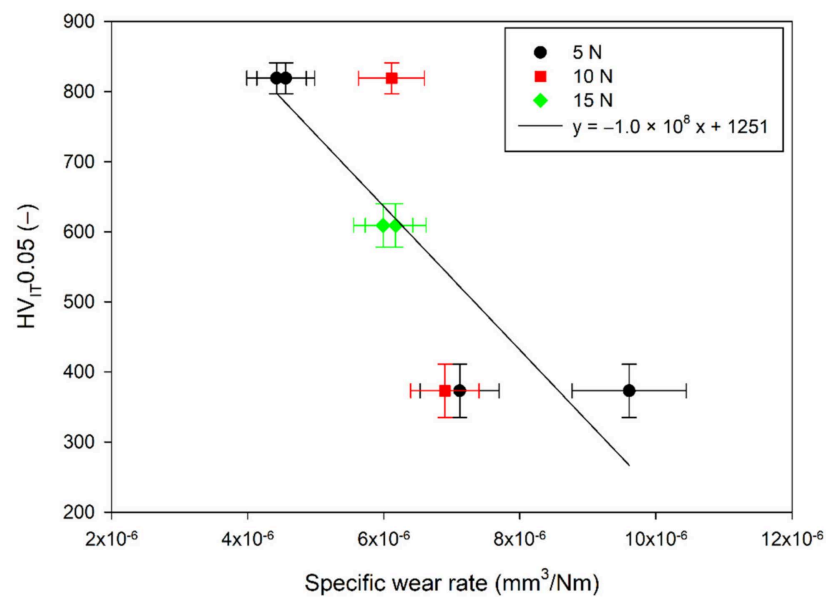


**Figure 13.** Dependence of specific wear rate and hardness with a linear fit.

### 3.7. Surface Finishing

Because laser cladding does not achieve adequate accuracy, depending on its applications, it is necessary to machine the surface to the required final shape. Therefore, the surface of the clad was ground using an oscillating surface grinder, where 1.7 mm from the contact was removed. In this section, the microstructure parameters, the surface state of the residual stress and the hardness of the ground surface are described. These values significantly affect the properties of the surface and thus the service life of the repaired part.

#### 3.7.1. Microstructure Parameters

The microstructure parameters are presented on the following maps (Figures 14–16), each of which consists of 33 values with linear interpolation between them. Figure 14 characterises the phase composition of the ground surface. Only ferrite (bcc phase) and retained austenite (fcc phase) were characterised on the surface by XRD quantitative phase analysis. The volume fraction of phase composition and microstructure parameters were also determined, where Figure 15 shows the crystallites size and Figure 16 the dislocation density. The error in calculating the volume fraction of ferrite was less than 0.1 wt. %; nevertheless, the total error of the phase analysis depends on many factors but was stated to be approximately 1 wt. %. The average crystallite size error was 0.8 nm and for dislocation density  $1.86 \times 10^{14} \text{ m}^{-2}$ .

The volume fraction of ferrite, and thus also the volume fraction of retained austenite, varied by up to 5 wt. %. From Figures 14–16, it is not possible to observe a certain correlation between the volume fraction of retained austenite, the size of the crystallites and dislocation density. Slightly higher values of crystallite size were in the left half of the ground surface (corresponded to the start of the cladding process) and, conversely, dislocation density was higher in the right. However, the values obtained showed a low standard deviation—1.2 nm and  $3.3 \times 10^{14} \text{ m}^{-2}$  which was almost comparable to the average error. Therefore, the ground surface appeared more homogeneous than the unground surface.

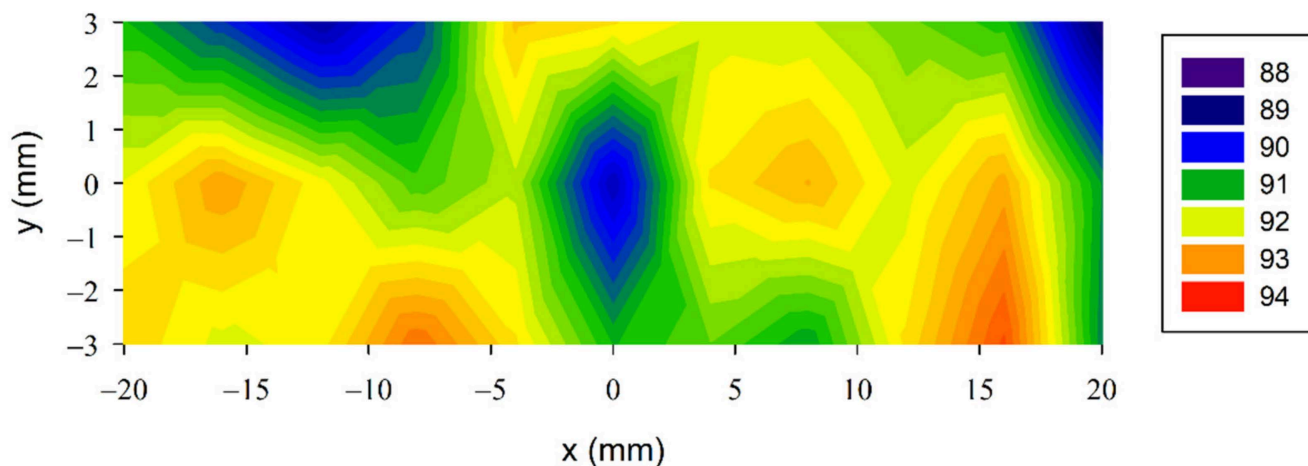


Figure 14. Map of the volume fraction of ferrite (bcc phase) on the ground surface of the clad.

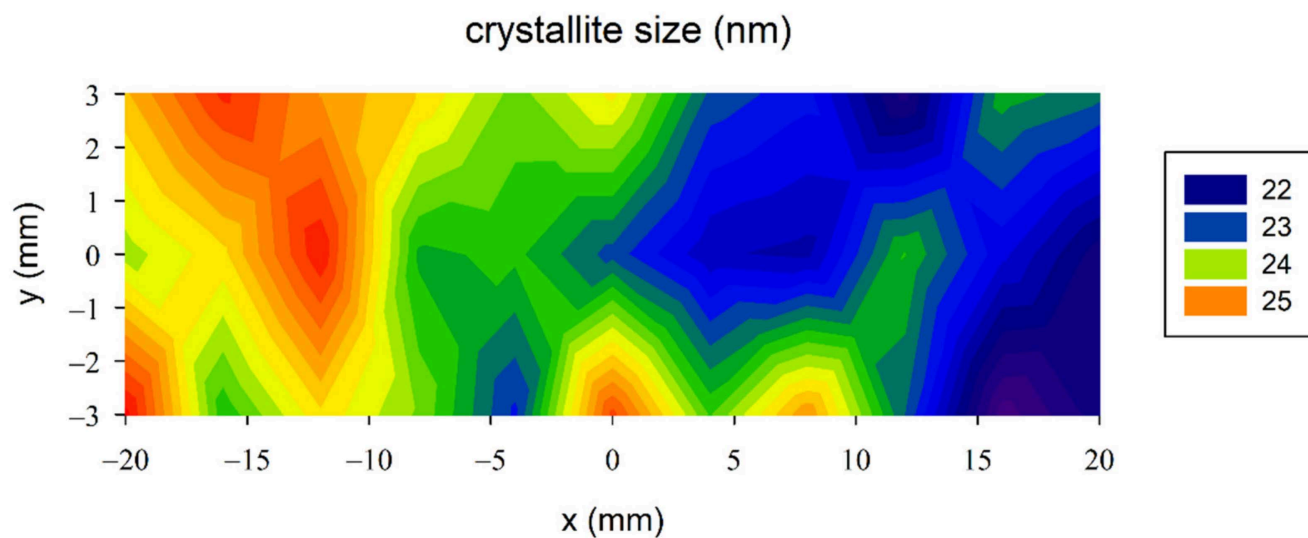


Figure 15. Map of crystallite size of ferrite (bcc phase) on the ground surface of the clad.

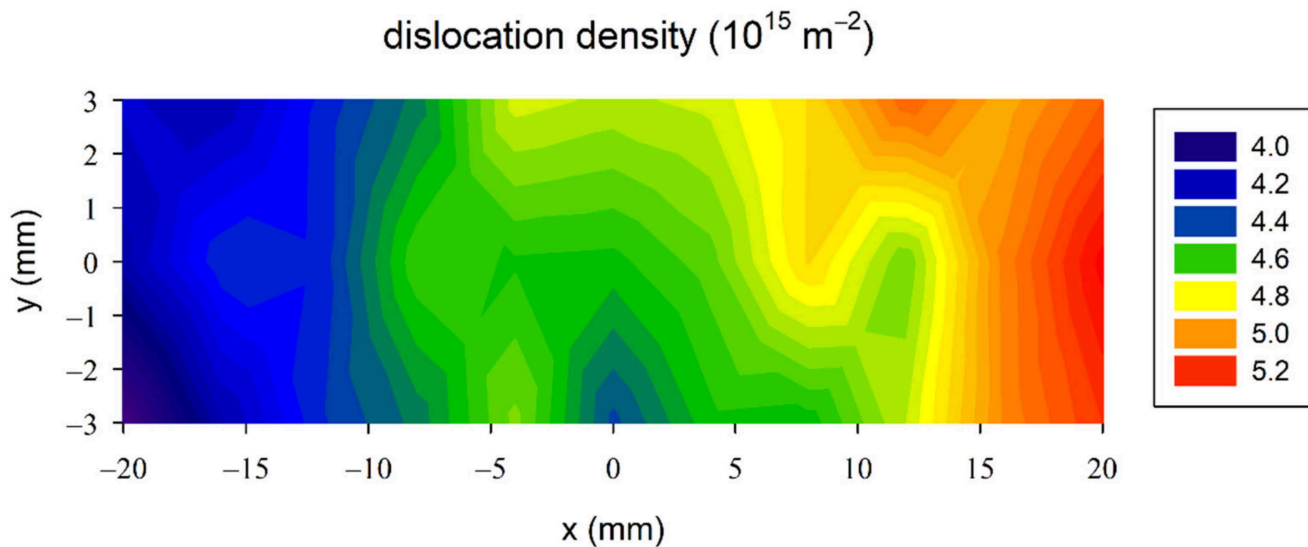
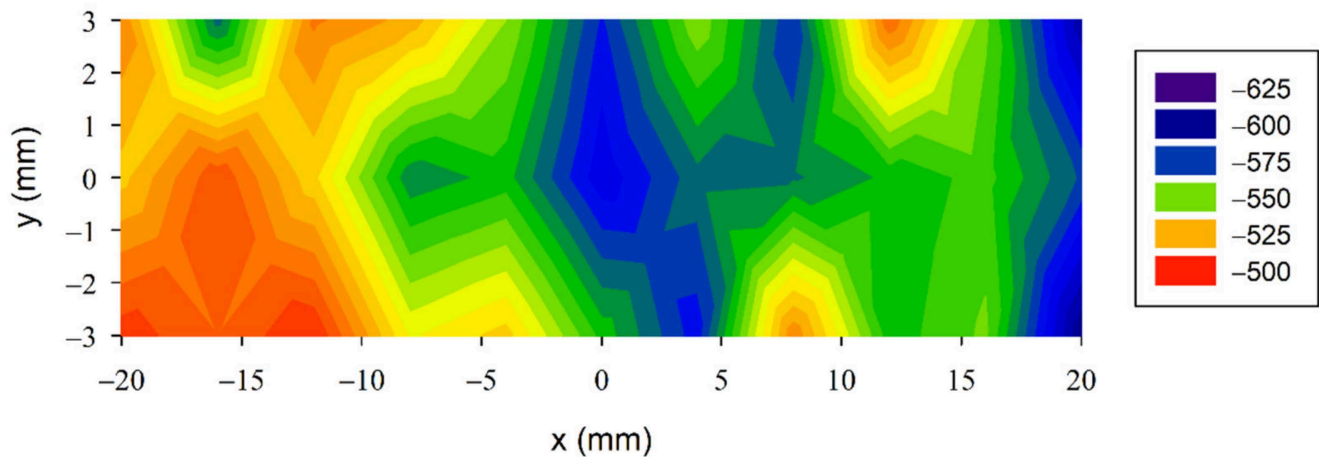


Figure 16. Map of dislocation density of ferrite (bcc phase) on the ground surface of the clad.

### 3.7.2. Surface Macroscopic Residual Stresses

Figures 17 and 18 characterize the surface macroscopic residual stresses of the ground surface in the L direction, i.e., in the cladding and grinding direction, and in the T direction, i.e., perpendicular. The average error of the residual stress calculation was 26 MPa for both directions.

#### residual stresses in L direction (MPa)



**Figure 17.** Map of surface macroscopic residual stresses on the ground surface of the clad in the L direction.

#### residual stresses in T direction (MPa)

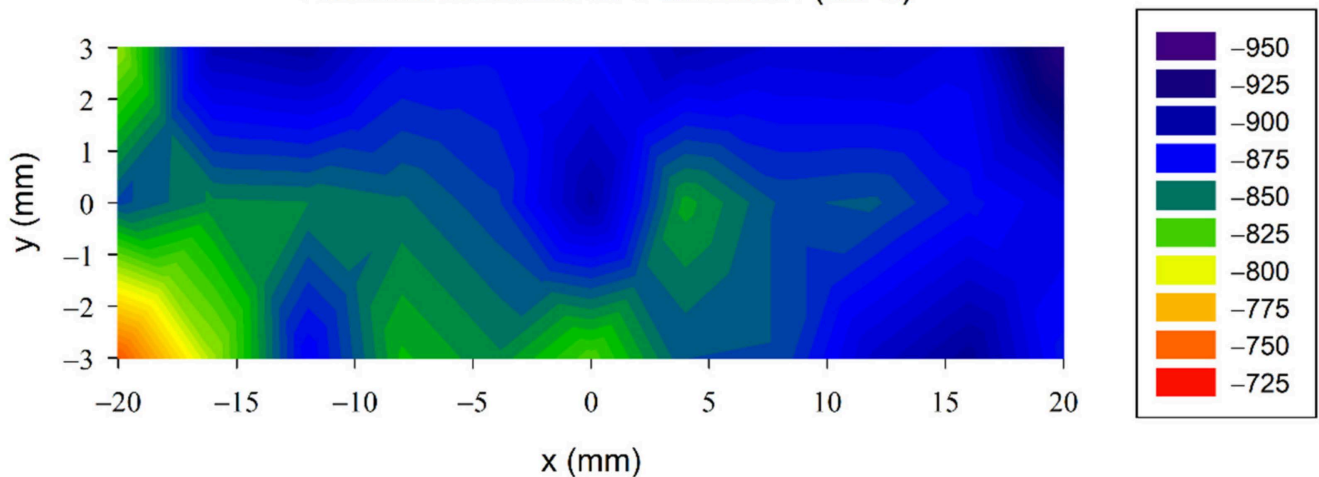


**Figure 18.** Map of surface macroscopic residual stresses on the ground surface of the clad in the T direction.

From the point of view of the development of residual stresses during grinding, the direction of grinding was unfavourable, i.e., in the L direction. The material was heavily plastically deformed in this direction during grinding, which can cause tensile residual stresses, especially if the depth of cut per pass is large and cooling is not sufficient [34]. However, only compressive residual stresses were analysed in both directions. In the L direction, as expected, the compressive residual stresses reached smaller values (−551 MPa with a standard deviation of 28 MPa vs. −867 MPa with a deviation of 34 MPa in T direction), but due to the small depth of cut per pass and sufficient cooling, tensile residual stresses did not occur.

It was also distinguishable that higher values of compressive stresses occurred in the right part of the clad for both directions. In the same area, the higher dislocation density

and the smaller crystallite size were determined, see Figures 15 and 16. This dependence is most likely caused by the cladding process, when the beads, from which the clad is made, end in the right part. Therefore, a different cooling rate probably occurred in this area.

### 3.7.3. Hardness

Figure 19 defines the hardness HV1 of the ground clad. The average hardness value was 681 HV1 with a standard deviation of 50 HV1. At a distance of approx.  $x = -15$  mm on the upper and lower side of the clad, the hardness reached only 535 HV1. The occurrence of an area with a lower hardness value on the surface of the repaired part is unfavourable in terms of its service life. Based on the previous results, it can be stated that the test specimens with lower hardness showed lower yield strength and, on average, a higher specific wear rate.

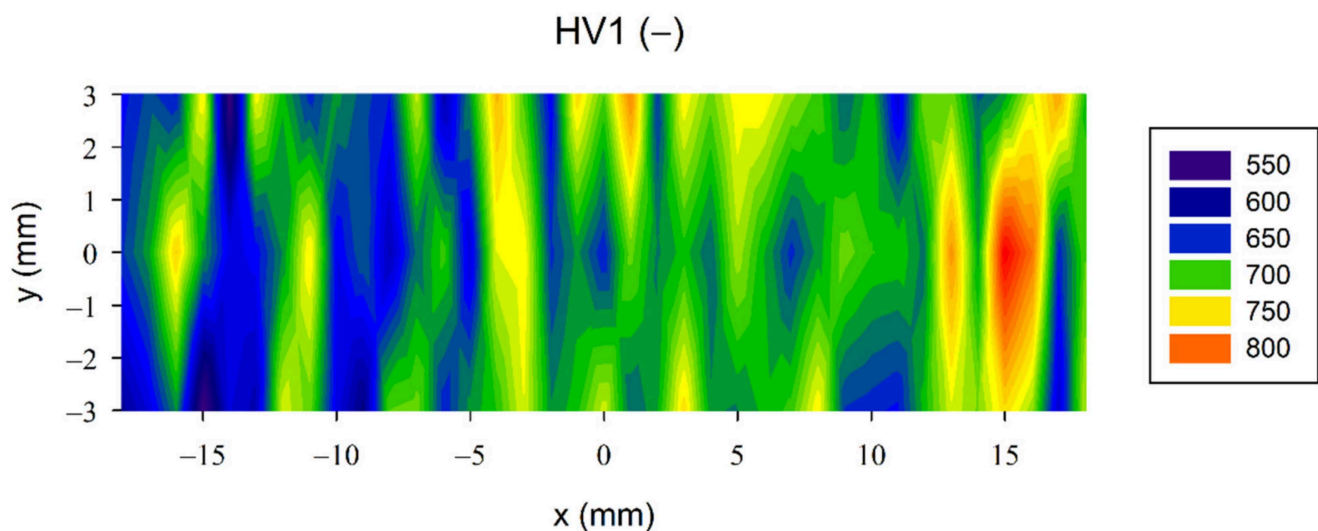


**Figure 19.** Hardness map of the ground surface of the clad.

It is also clear from Figure 19 that the higher hardness values were in the right part of the clad. Although the differences between dislocation density values and crystallite size were small, it was possible to observe that areas with higher hardness values correlated with areas with higher dislocation density and smaller crystallite size. Yield stress (represented by hardness) increased with increasing dislocation density  $\rho$  (following a  $\rho^{1/2}$  relationship) and with decreasing grain size  $d$  (according to Hall–Petch effect following a  $d^{-1/2}$  relationship) since the crystallite size often correlates with the grain size. It is important to note that for ductile failure during wear, the determining fracture is not just yield stress but also toughness following a  $d^{-1}$  relationship upon decreasing grain size (the strength of the toughness effect is correlated to the difference in fracture toughness between grain boundary and grain interior toughness) [35]. In the area with higher hardness, the compressive residual stresses also reached higher values in both directions.

When optimizing the parameters of laser cladding in the future production process, it would be appropriate from the point of view of service life to achieve the parameters that occur in the right part of the clad, where the beads always end during the cladding process. This fact would be appropriate to investigate in further research using numerical methods.

## 4. Conclusions

The knowledge obtained from the experiments can be summarised in the following bullet points:

- It was found that the clad layers showed differences in microstructure across the thickness that may lead to undesirable properties;

- Martensitic structure predominated, but a mostly ferritic structure was observed in the second clad layer. It was confirmed that this area had a significantly lower hardness by about 200 HV. The decrease in hardness corresponded to annealing to a temperature of approximately 600 °C;
- The majority of alloying elements in the clad were not in the form of carbides. Carbides were confirmed only in the area with a mostly ferritic structure;
- A crack was observed on the surface of the clad, its propagation could be supported by tensile surface residual stresses in the T direction. The bulk compressive residual stresses in the T direction were characterised only at the interface between the clad and the base material;
- Surface residual stresses reached mainly compressive values in the L direction; only at the edges, there were areas with tensile stresses. However, unfavourable bulk tensile stresses were determined using neutron diffraction in the clad in the L direction;
- The resulting wear resistance of the clad was significantly affected by the hardness of the functional surface. In turn, it was shown that the hardness was significantly affected by the cladding process and also by the temperature reached during the cladding of the subsequent layers;
- The outer surface layer, which showed tensile surface residual stresses and cracks, was removed by grinding. Furthermore, surface compressive residual stresses were described in both directions on the ground surface, which is convenient from the point of view of component service life.

From these findings, it can be concluded that the strategy of the cladding process and temperature control can significantly affect the resulting material properties. Further, the description of the formation of areas with lower hardness needs to be paid attention to in further research.

**Author Contributions:** Conceptualization, K.T., V.O. and N.G.; methodology, investigation, data curation, and visualization K.T., V.O., J.Č. (Jiří Čapek), J.Č. (Jaroslav Čech), D.C.-Y. and K.K.; writing—original draft preparation, K.T.; writing—review and editing, K.T., V.O., J.Č. (Jiří Čapek), J.Č. (Jaroslav Čech), D.C.-Y., N.G. and J.T.M.D.H.; supervision and project administration, V.O. and N.G.; funding acquisition, V.O., N.G. and J.T.M.D.H. All authors have read and agreed to the published version of the manuscript.

**Funding:** This research was funded by the Center for Advanced Applied Science, grant number CZ.02.1.01/0.0/0.0/16\_019/0000778. “Center for Advanced Applied Science” within the Operational Program Research, Development and Education supervised by the Ministry of Education, Youth and Sports of the Czech Republic. The authors acknowledge the CANAM infrastructure of the NPI ASCR Řež supported through the Ministry of Education, Youth, and Sports Project No. LM2015056 as well as the infrastructure Reactors LVR-15 and LR-0 supported by Project LM2018120 of the Ministry of Education, Youth, and Sports of the Czech Republic. K.T.’s work was supported by the Grant Agency of the Czech Technical University in Prague, grant number SGS19/190/OHK4/3T/14.

**Institutional Review Board Statement:** Not applicable.

**Informed Consent Statement:** Not applicable.

**Data Availability Statement:** Data sharing is not applicable to this article.

**Conflicts of Interest:** The authors declare no conflict of interest.

## References

1. Steen, W.M. *Laser Material Processing*, 3rd ed.; Springer: London, UK, 2003; pp. 349–369.
2. Ocelík, V.; De Hosson, J.T.M. Thick metallic coatings by coaxial and side laser cladding: Processing and properties. In *Advances in Laser Materials Processing Technology*; Schaaf, P., Ed.; Woodhead Publishing Ltd.: Oxford, UK; CRC Press: West Palm Beach, FL, USA, 2010; pp. 426–458.
3. Telasang, G.; Majumdar, J.D.; Wasekar, N.; Padmanabham, G.; Manna, I. Microstructure and mechanical properties of laser clad and post-cladding tempered AISI H13 tool steel. *Metall. Mater. Trans. A* **2015**, *46*, 2309–2321. [[CrossRef](#)]

4. Shinde, M.S.; Ashtankar, K.M. Additive manufacturing–assisted conformal cooling channels in mold manufacturing processes. *Adv. Mech. Eng.* **2017**, *9*, 1–14. [[CrossRef](#)]
5. Vedani, M.; Previtali, B.; Vimercati, G.M.; Sanvito, A.; Somaschini, G. Problems in laser repair-welding a surface-treated tool steel. *Surf. Coat. Technol.* **2007**, *201*, 4518–4525. [[CrossRef](#)]
6. Zhu, L.; Wang, S.; Pan, H.; Yuan, C.; Chen, X. Research on remanufacturing strategy for 45 steel gear using H13 steel powder based on laser cladding technology. *J. Manuf. Process.* **2020**, *49*, 344–354. [[CrossRef](#)]
7. Zhao, X.; Lv, Y.; Dong, S.; Yan, S.; He, P.; Liu, X.; Liu, Y.; Lin, T.; Xu, B. The effect of thermal cycling on direct laser-deposited gradient H13 tool steel: Microstructure evolution, nanoprecipitation behaviour, and mechanical properties. *Mater. Today Commun.* **2020**, *25*, 101390. [[CrossRef](#)]
8. Roberts, G.A.; Kennedy, R.; Krauss, G. *Tool Steels*, 5th ed.; ASM International: Materials Park, OH, USA, 1998; pp. 67–107.
9. Schwartz, R.A.; Field, D.P.; Adams, B.L.; Kumar, M.; Schwartz, A.J. Present state of electron backscatter diffraction and prospective developments. In *Electron Backscatter Diffraction in Materials Science*; Springer: Boston, MA, USA, 2009; pp. 1–20.
10. Candel, J.J.; Amigó, V.; Ramos, J.A.; Busquets, D. Problems in laser repair cladding a surface AISI D2 heat-treated tool steel. *Weld. Int.* **2013**, *27*, 10–17. [[CrossRef](#)]
11. Ferreira, D.F.; Vieira, J.S.; Rodrigues, S.P.; Miranda, G.; Oliveira, F.J.; Oliveira, J.M. Dry sliding wear and mechanical behaviour of selective laser melting processed 18Ni300 and H13 steels for moulds. *Wear* **2022**, *488*, 204179. [[CrossRef](#)]
12. Köhler, H.; Partes, K.; Kornmeier, J.R.; Vollertsen, F. Residual stresses in steel specimens induced by laser cladding and their effect on fatigue strength. *Phys. Procedia* **2012**, *39*, 354–361. [[CrossRef](#)]
13. Bhadeshia, H.K.D.H. Effect of materials and processing: Material factors. In *Handbook of Residual Stress and Deformation of Steel*; Totten, G., Howes, M., Inoue, T., Eds.; ASM International: Materials Park, OH, USA, 2002; pp. 3–10.
14. Cottam, R.; Wang, J.; Luzin, V. Characterization of microstructure and residual stress in a 3D H13 tool steel component produced by additive manufacturing. *J. Mater. Sci. Res.* **2014**, *29*, 1978–1986. [[CrossRef](#)]
15. Bailey, N.S.; Katinas, C.; Shin, Y.C. Laser direct deposition of AISI H13 tool steel powder with numerical modeling of solid phase transformation, hardness, and residual stresses. *J. Mater. Process. Technol.* **2017**, *247*, 223–233. [[CrossRef](#)]
16. Chen, J.; Wang, S.; Xue, L. On the development of microstructures and residual stresses during laser cladding and post-heat treatments. *J. Mater. Sci.* **2012**, *47*, 779–792. [[CrossRef](#)]
17. Nenadl, O.; Kuipers, W.; Koelewijn, N.; Ocelík, V.; De Hosson, J.T.M. A versatile model for the prediction of complex geometry in 3D direct laser deposition. *Surf. Coat. Technol.* **2016**, *307*, 292–300. [[CrossRef](#)]
18. Trojan, K.; Ocelík, V.; Ganeev, N.; Němeček, S.; Čapek, J. Effects of advanced laser processing on the microstructure and residual stresses of H13 tool steel. In Proceedings of the 55th International Scientific Conference on Experimental Stress Analysis 2017, Nový Smokovec, Slovakia, 30 May–1 June 2017; pp. 464–471.
19. ISO 14577. *Metallic Materials—Instrumented Indentation Test for Hardness and Material Parameters*; ISO: Geneva, Switzerland, 2002.
20. Oliver, W.C.; Pharr, G.M. Measurement of hardness and elastic modulus by instrumented indentation: Advances in understanding and refinements to methodology. *J. Mater. Res.* **2004**, *19*, 3–20. [[CrossRef](#)]
21. Leoni, M. Whole powder pattern modelling: Microstructure determination from powder diffraction data. In *International Tables for Crystallography, Volume H, Powder Diffraction*; Gilmore, C.J., Kaduk, J.A., Schenk, H., Eds.; Wiley: Hoboken, NJ, USA, 2019; pp. 288–303.
22. *Orientation Imaging Microscopy (OIM)*; Software Version 7.3.0; User Manual; TSL, TexSEM Laboratories: Draper, UT, USA, 2015.
23. Matěj, Z.; Kužel, R. MStruct—Software/Library for MicroStructure Analysis by Powder Diffraction. Available online: <http://www.xray.cz/mstruct/> (accessed on 10 October 2021).
24. Williamson, G.K.; Smallman, R.E.III. Dislocation densities in some annealed and cold-worked metals from measurements on the X-ray debye-scherrer spectrum. *Philos. Mag.* **1956**, *1*, 34–46. [[CrossRef](#)]
25. Von Dreele, R.B. Powder diffraction peak profiles. In *International Tables for Crystallography, Volume H, Powder Diffraction*; Gilmore, C.J., Kaduk, J.A., Schenk, H., Eds.; Wiley: Hoboken, NJ, USA, 2019; pp. 263–269.
26. Murray, C.E.; Noyan, I.C. Applied and residual stress determination using X-ray diffraction. In *Practical Residual Stress Measurement Methods*; Schajer, G.S., Ed.; John Wiley & Sons: Chichester, UK, 2013; pp. 139–161.
27. Mikula, P.; Vrana, M. High-resolution neutron diffraction for phase and residual stress investigations. In *Fracture of Nano and Engineering Materials and Structures*; Gdoutos, E.E., Ed.; Springer: Dordrecht, The Netherlands, 2006. [[CrossRef](#)]
28. Randau, C.; Garbe, U.; Brokmeier, H.G. StressTextureCalculator: A software tool to extract texture, strain and microstructure information from area-detector measurements. *J. Appl. Crystallogr.* **2011**, *44*, 641–646. [[CrossRef](#)]
29. Holden, T.M. Neutron diffraction. In *Practical Residual Stress Measurement Methods*; Schajer, G.S., Ed.; John Wiley & Sons: Chichester, UK, 2013; pp. 195–223.
30. Wern, H.; Johannes, R.; Walz, H. Dependence of the X-ray elastic constants on the diffraction plane. *Phys. Status Solidi* **1998**, *206*, 545–557. [[CrossRef](#)]
31. Chen, C.; Yan, K.; Qin, L.; Zhang, M.; Wang, X.; Zou, T.; Hu, Z. Effect of heat treatment on microstructure and mechanical properties of laser additively manufactured AISI H13 tool steel. *J. Mater. Eng. Perform.* **2017**, *26*, 5577–5589. [[CrossRef](#)]

32. Mikami, Y.; Oda, K.; Kamaya, M.; Mochizuki, M. Effect of reference point selection on microscopic stress measurement using EBSD. *Mater. Sci. Eng.* **2015**, *647*, 256–264. [[CrossRef](#)]
33. Dao, M.; Lu, L.; Asaro, R.J.; De Hosson, J.T.M.; Ma, E. Toward a quantitative understanding of mechanical behavior of nanocrystalline metals. *Acta Mater.* **2007**, *55*, 4041–4065. [[CrossRef](#)]
34. Rowe, W.B. Thermal damage. In *Principles of Modern Grinding Technology*, 2nd ed.; Rowe, W.B., Ed.; William Andrew Publishing: Oxford, UK, 2013; pp. 113–122.
35. Fan, Z. The grain size dependence of ductile fracture toughness of polycrystalline metals and alloys. *Mater. Sci. Eng. A* **1995**, *191*, 73–83. [[CrossRef](#)]